Journal of Applied Fluid Mechanics, Vol. 18, No. 6, pp. 1381-1395, 2025.
Available online at www.jafmonline.net, ISSN 1735-3572, EISSN 1735-3645.
https://doi.org/10.47176/jafm.18.6.3218

Research on Axisymmetric Vectoring Exhaust Nozzle Dynamic Characteristics Considering Aerodynamic and Thermal Loads Effect

S. Yao[1,2], Z. Luo[1,2,3†], H. Zhang[1,2], C. Xu[4], H. Ji[1,2] and C. Pang[1,2]

[1] *School of Mechanical Engineering & Automation, Northeastern University, Shenyang, Liaoning, 110819, China*
[2] *Key Laboratory of Vibration and Control of Aero-Propulsion System, Northeastern University, Shenyang, Liaoning, 110819, China*
[3] *Foshan Graduate School of Innovation, Northeastern University, Foshan, Guangdong, 528312, China*
[4] *AECC Shenyang Engine Research Institute, Shenyang, Liaoning, 110015, China*

†*Corresponding Author Email: zhluo@mail.neu.edu.cn*

ABSTRACT

The Axisymmetric Vectoring Exhaust Nozzle (AVEN) has been extensively studied in thrust vectoring technology due to its ability to achieve 360° vector deflection. A key observation is that thermal loads are closely linked to joint clearance, which introduces significant complexity and unpredictability to the system's dynamic response. This paper investigates the impact of thermal loads on joint forces using a finite element model. A fluid field analysis method was developed based on the operational conditions of the AVEN. The inner wall temperature obtained from this fluid analysis was then used as a boundary condition in the structural thermal analysis model. The results indicate that, for the relative angle of the joint, the combined aerodynamic and thermal loads contribute to the total aerodynamic-thermal interaction effects. Furthermore, structural stress in the steering control ring segment is primarily influenced by aerodynamic loads, while the convergence regulator ring segment is mainly affected by thermal loads.

Article History

Received October 22, 2024
Revised December 11, 2024
Accepted January 14, 2025
Available online March 30, 2025

Keywords:

Axialsymmetric vectoring exhaust nozzle
Thermal analysis
Vector deflection
Dynamic analysis
Stress analysis

1. INTRODUCTION

The Axisymmetric Vectoring Exhaust Nozzle (AVEN) can achieve a 360° vector deflection, significantly enhancing jet maneuverability and reducing takeoff speed, making it a central focus of thrust vectoring technology (Wang, 2006). Current research on AVEN primarily focuses on single physical fields, often overlooking the impact of thermal loads on its structure (Li & Wang, 2014; Gao et al. 2021; Wang et al., 2011). Furthermore, aerodynamic loads are typically simplified as equivalent loads rather than being modeled as distributed loads. Since AVEN operates under both aerodynamic and thermal loads in real-world conditions, investigating its dynamic characteristics while incorporating thermal load effects is crucial for practical applications.

Currently, limited studies have examined the effects of thermal load on the AVEN (Yao et al., 2022). However, numerous publications have investigated multi-physics interactions in other mechanisms, such as thrust nozzles (Wang et al., 2019; Zhou et al., 2022; Zhang et al., 2024), rocket engines (Alimohammadi & Aghaei-Togh 2023; Bahamon & Martinez 2023; Cheng et al., 2023), turbines (Rogowski et al., 2018; Tahani & Moradi, 2016), and ejectors (Lijo et al., 2010a; Luo et al., 2021). Focusing on the converging-diverging nozzle, Liu et al. (2022) developed a computational algorithm to address fluid-solid interaction problems, incorporating temperature effects, and validated its reliability. Gao et al. (2022) used numerical simulations to study the influence of operational pressure on the nozzle's heat release characteristics. Liu et al. (2005) applied simplified chemical reaction mechanisms and large eddy simulation (LRS) to examine non-equilibrium fluid characteristics within nozzles, highlighting the impact of wall roughness on fluid field behavior. Pizzarelli et al. (2009, 2014, 2024) conducted extensive research on the multi-physics interactions in liquid rocket engines (LREs). In 2007, they developed a computational fluid dynamics (CFD) code to simulate methane as a coolant, based on observed fluid properties in LREs. They later proposed a numerical method for calculating two-dimensional axisymmetric fluid fields in a trans-critical state. In 2009, they modeled supercritical fluid turbulence, emphasizing differences between supercritical fluids and ideal gases, and analyzed wall heat flux evolution in detail. Between 2011 and 2014, a quasi-two-dimensional model for LREs was introduced, enabling rapid predictions of coolant flow

NOMENCLATURE

A	fluid cross-sectional area	u_τ	wall shear velocity
$C_{1\varepsilon}$	constant	v	fluid velocity
$C_{2\varepsilon}$	constant	x_i	displacement component
$C_{3\varepsilon}$	constant term	x_{Ni}	relative position of the ith mechanism with no load
C_f	constant term	x_{PTi}	relative position of the ith mechanism with the action of aerodynamic and thermal loads
C_μ	constant	$\triangle x_{Pi}$	relative position of the ith mechanism with the action of aerodynamic load
$\boldsymbol{C}^t$	temperature-velocity matrix	$\triangle x_{Ti}$	relative position of the ith mechanism with the action of thermal load
$\boldsymbol{C}^{tq}$	temperature-damping matrix	y_S^+	location at which the log-law slope is fixed
d	fluid characteristic length	Y_M	contribution of the fluctuating dilatation in compressible turbulence to the overall dissipation rate
E_G	elastic modulus of gh4099	α	pressure gradient influence coefficient
$\boldsymbol{F}^{th}$	temperature external load matrix	α_G	coefficient of linear expansion
G_κ	turbulent kinetic energy generated by the average velocity gradient	α_k	inverse effective Prandtl number for the turbulent kinetic energy k
G_b	turbulent kinetic energy generated by buoyancy	α_ε	inverse effective Prandtl number of the dissipation rate ε
k	turbulent kinetic energy	β_1	constant
k_i	thermal conductivity in the i direction	β_2	thermal effect coefficient
$\boldsymbol{K}^t$	temperature-stiffness matrix	γ	thermal effect coefficient
$\boldsymbol{K}^{tq}$	temperature-velocity matrix	δ_0	thickness of the first boundary layer
M	fluid mass flow	δ_e	calculation error
N	total number of boundary layers	δ_{tot}	total thickness of the boundary layer
$\boldsymbol{Q}$	energy matrix	ε	dissipation rate
$\boldsymbol{Q}^{th}$	external energy load matrix	η_0	constant
r	growth rate of the boundary layer	κ	von Kármán constant
S	Sutherland constant	λ_G	thermal conductivity
S_1	total entropy	μ	dynamic viscosity
S_k	source term	μ_0	fluid dynamic viscosity at 273 k
S_ε	source term	μ_{eff}	effective turbulent viscosity
T	temperature	μ_G	Poisson's ratio
T^*	temperature of the inner wall of the nozzle	μ_t	turbulent viscosity
$\boldsymbol{T}$	temperature matrix	ρ	fluid density
u_i	fluid velocity component	τ_w	wall shear stress

and cooling channel temperature characteristics. Using the Spalart-Allmaras (SA) turbulence model, they conducted numerical calculations incorporating wall heat conduction and coolant flow, investigating the effects of structural parameters and aspect ratios on fluid dynamics and heat transfer. From 2015 to 2024, their studies expanded to include 3D conjugate heat transfer simulations, addressing coolant pressure and wall roughness while identifying heat transfer deterioration phenomena in supercritical fluids. To address the "doghouse" damage failure observed in LREs, Kowollik et al. (2013) proposed a viscous-plastic damage model to describe material behavior under cyclic thermal loads. Xiang & Sun (2018, 2020) performed numerical calculations of coupled film cooling heat transfer in LOX/GH2 thrust chambers. Their findings showed that tangential angles reduced average recirculation area temperatures and enhanced film cooling performance near injectors, while azimuthal angles minimized temperature non-uniformity on the hot gas sidewall circumferentially. Additionally, Lijo et al. (2010b) and Edathol et al. (2020) conducted numerical simulations on thrust-optimized contour nozzles under two flow separation phenomena. Their comparative analysis of five nozzles using density and pressure solvers provided valuable insights into nozzle performance under varying conditions.

In summary, the discussions primarily focus on the fluid field and heat transfer characteristics (Chen et al., 2018; Zhou et al., 2020). However, research on the dynamic characteristics of the AVEN remains limited, particularly regarding the importance of thermal loads in accurately predicting dynamic responses. To address this gap, this study investigates the AVEN as the research object. An approximate model simplification method is employed to develop a simplified fluid field model, complemented by the construction of a comprehensive three-dimensional model. Leveraging weak interaction theory, CFD, and thermodynamics, a dynamic model of the AVEN that incorporates aerodynamic and thermal load effects is established. The study further analyzes the impact of these loads on the dynamic response.

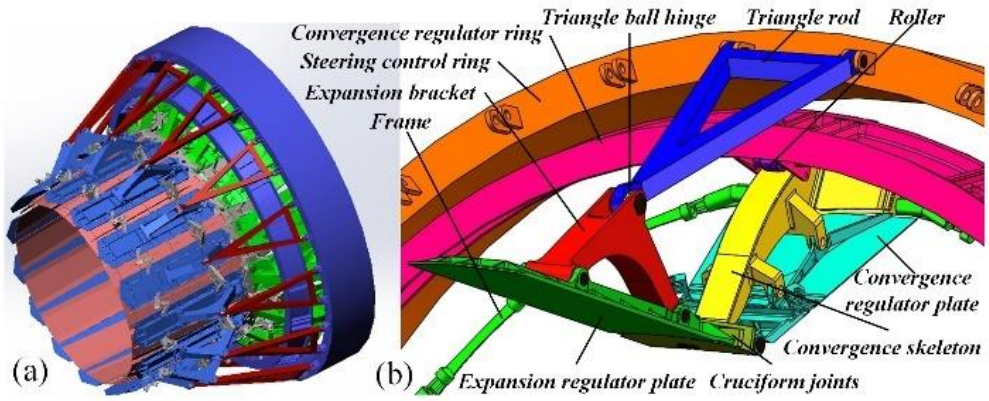

Fig. 1 Structure diagram of AVEN (a) Overall assembly (b) Main components

Table 1 Main parameters of GH4099

T (K)	E_G (GPa)	μ_G	λ_G ($W/(m\cdot K)$)	α_G (10^{-6} K)
293.15	223	0.37	10.47	12
313.15	219	0.37	10.47	12
413.15	215	0.36	12.56	12.4
513.15	210	0.37	14.24	12.8
613.15	205	0.36	15.91	13
713.15	199	0.36	18.00	13.7
813.15	194	0.35	19.68	14.2
913.15	184	0.30	21.77	14.7
1013.15	178	0.33	23.45	15.1
1113.15	164	0.36	25.54	15.3
1213.15	147	0.36	27.21	17.4

2. PHYSICAL MODEL AND NUMERICAL METHOD

2.1 Physical Model

Figure 1 is the structure diagram of AVEN in thispaper. The material is nickel-based material GH4099, its density is 8470 kg/m^3. Table 1 (Yan, 2002) is the main parameter.

2.2 Governing Equations

(1) Governing equations for fluid field analysis (Christophe, 2018)

A suitable turbulence model can be selected according to the Reynolds number (Re), namely:

$$\mathrm{Re}=\frac{\rho v d}{\mu} \tag{1}$$

where:

$$v=\frac{M}{A\rho} \tag{2}$$

$$\mu=\mu_0\frac{273+S}{T+S}\left(\frac{T}{273}\right)^{\frac{3}{2}} \tag{3}$$

Table 2 Working conditions

Object	Parameter
Inlet mass flow (kg/s)	124
Total inlet pressure (Mpa)	0.29
Inlet temperature (K)	766
Inlet diameter (m)	0.81
Throat diameter (m)	0.5

The actual working conditions of AVEN are as shown in Table 2, and the outlet is the ambient pressure and temperature. The mixed gas composition is N_2, CO_2, and H_2O, the proportion is 70.6%, 20.9%, and 8.5% respectively, the mixed gas density is about 1.205 kg/m^3.

The Re is calculated using Eqs. (1) to (3) and is approximately 1×10^7. While turbulence models like the k-ω turbulence model or LES offer greater accuracy, they require significantly higher computational resources, particularly in complex geometries where the demand increases exponentially. Considering that the primary objective of this research is to analyze qualitative fluid field trends and pressure distributions through numerical simulations, the RNG k-ε turbulence model is selected for fluid field calculations (Li et al., 2017; Nie et al., 2022), as follows:

$$\frac{\partial}{\partial t}(\rho k)+\frac{\partial}{\partial x_i}(\rho k u_i)=\frac{\partial}{\partial x_j}\left(\alpha_k\mu_{eff}\frac{\partial k}{\partial x_j}\right)+G_k+G_b-\rho\varepsilon-Y_M+S_k \tag{4}$$

$$\frac{\partial}{\partial t}(\rho\varepsilon)+\frac{\partial}{\partial x_i}(\rho\varepsilon u_i)=\frac{\partial}{\partial x_j}\left(\alpha_\varepsilon\mu_{eff}\frac{\partial\varepsilon}{\partial x_j}\right)+ C_{1\varepsilon}\frac{\varepsilon}{k}(G_k+C_{3\varepsilon}G_b)-C_{2\varepsilon}\rho\frac{\varepsilon^2}{k}+R_\varepsilon+S_\varepsilon \tag{5}$$

where:

$$R_\varepsilon=\frac{C_\mu\rho\eta^3\left(1-\frac{\eta}{\eta_0}\right)}{1+\beta_1\eta^3}\frac{\varepsilon^2}{k} \tag{6}$$

$$\eta\equiv\frac{S_1 k}{\varepsilon} \tag{7}$$

$$\mu_{eff}=\mu_t=\rho C_\mu\frac{\kappa^2}{\varepsilon} \tag{8}$$

The enhanced wall function, as described in previous papers (Wolfshtein 1969; Chen & Patel 1988; Jongen 1992), which incorporates pressure gradient and thermal effects into its calculations, is utilized, namely:

$$\frac{du_t^+}{dy^+}=\frac{1}{\kappa y^+}\sqrt{S\left[1-\beta_2 u^+-\gamma\left(u^+\right)^2\right]} \tag{9}$$

where:

$$S=\begin{cases}1+\alpha y^+ & for \quad y^+<y_S^+\\ 1+\alpha y_S^+ & for \quad y^+\geq y_S^+\end{cases} \tag{10}$$

The no-slip boundary condition was applied to the fluid-structure interaction surface, while the wall boundary condition was used for the inner and outer walls of the solid. Additionally, the thermal condition was set to represent convection.

(2) Governing Equations for Structural Thermal Analysis (Li, 2009).

The structural thermal analysis of the AVEN mechanism was treated as a steady-state heat transfer problem. Assuming the components have constant properties and no internal heat sources, the governing equation is as follows:

$$\frac{\partial}{\partial x_i}\left(k_i\frac{\partial \boldsymbol{T}}{\partial x_i}\right)=0 \tag{11}$$

where:

$$i=x,y,z \tag{12}$$

Dirichlet condition is adopted by the heat conduction boundary condition, namely:

$$\boldsymbol{T}=T^* \tag{13}$$

(3) Governing equations for dynamic analysis

There are two primary types of thermal-structure interaction: strong interaction and weak interaction (Zhang & Hisada 2004; Li et al., 2021).

Strong interaction incorporates the interaction effect directly into the governing equation by modifying the element matrix or load vector. The governing equation is then solved accordingly, as follows:

$$\begin{bmatrix}\boldsymbol{M} & 0\\ 0 & 0\end{bmatrix}\begin{bmatrix}\boldsymbol{q}''\\ \boldsymbol{T}''\end{bmatrix}+\begin{bmatrix}\boldsymbol{C} & 0\\ \boldsymbol{C}^{tq} & \boldsymbol{C}^{t}\end{bmatrix}\begin{bmatrix}\boldsymbol{q}'\\ \boldsymbol{T}'\end{bmatrix}+\begin{bmatrix}\boldsymbol{K} & \boldsymbol{K}^{qt}\\ 0 & \boldsymbol{K}^{t}\end{bmatrix}\begin{bmatrix}\boldsymbol{q}\\ \boldsymbol{T}\end{bmatrix}=\begin{bmatrix}\boldsymbol{F}\\ \boldsymbol{Q}\end{bmatrix} \tag{14}$$

The weak interaction is the interaction of two fields by applying the result of the first physics field as an external load to the second physics field, namely:

$$\begin{bmatrix}\boldsymbol{M} & 0\\ 0 & 0\end{bmatrix}\begin{bmatrix}\boldsymbol{q}''\\ \boldsymbol{T}''\end{bmatrix}+\begin{bmatrix}\boldsymbol{C} & 0\\ 0 & \boldsymbol{C}^{t}\end{bmatrix}\begin{bmatrix}\boldsymbol{q}'\\ \boldsymbol{T}'\end{bmatrix}+\begin{bmatrix}\boldsymbol{K} & 0\\ 0 & \boldsymbol{K}^{t}\end{bmatrix}\begin{bmatrix}\boldsymbol{q}\\ \boldsymbol{T}\end{bmatrix}=\begin{bmatrix}\boldsymbol{F}+\boldsymbol{F}^{th}\\ \boldsymbol{Q}+\boldsymbol{Q}^{ted}\end{bmatrix} \tag{15}$$

2.3 Confirmatory Calculation

To validate the mathematical model proposed in this study, a Converging-Diverging nozzle (Back et al.,1964; Liu et al., 2005) was selected as the verification object, and a three-dimensional physical model of the nozzle was developed. A numerical simulation was then performed, and the results were compared with experimental data to assess the model's accuracy. The Converging-Diverging nozzle, characterized as axisymmetric, has the following structural parameters: a throat diameter of 45.8 mm, a contraction-area ratio of 7.75:1, an expansion-area ratio of 2.68:1, a convergent half-angle of 30°, and a divergent half-angle of 15°. The working conditions are as follows: the total inlet pressure is 0.5171 MPa, the total inlet temperature is 843.33 K, and the outlet is set to ambient temperature and pressure. Additionally, the outer wall temperature varies with position, as illustrated in Fig. 2 (Back et al. ,1964; Liu et al., 2005). The material of the nozzle is AISI 316, with key properties including a density of 8238 kg/m³, a specific heat capacity of 504 J/(kg·K), and a thermal conductivity of 15.2 W/(m·K). The meshing of the near-wall region was designed to satisfy $y^+\leq 5$ or $30\leq y^+\leq 300$. To optimize computational efficiency, this study adopted the range $30\leq y^+\leq 300$, ensuring y^+ values are as close to 30 as possible. Based on this criterion, the thickness of the first boundary layer and the total number of boundary layers were estimated preliminarily (Schlichting & Gersten 2017).

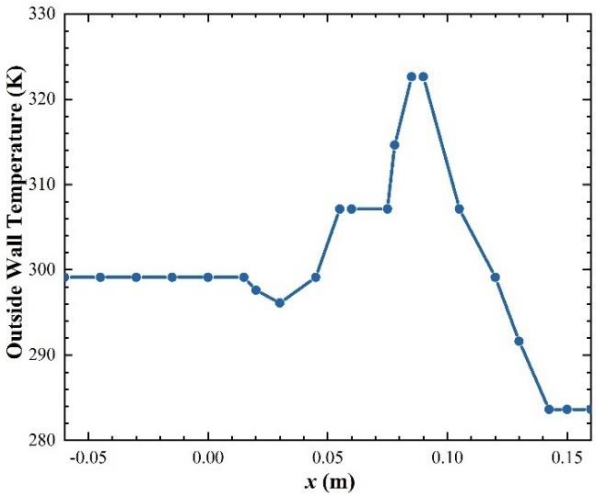

Fig. 2 Outside wall temperature of Converging-Diverging nozzle

The thickness of the first boundary layer can be calculated as follows:

$$C_f=\left[2\lg(Re)-0.65\right]^{-2.3} \tag{16}$$

$$\tau_w=C_f\cdot\frac{1}{2}\rho v^2 \tag{17}$$

$$u_\tau=\sqrt{\frac{\tau_w}{\rho}} \tag{18}$$

$$\delta_0=\frac{y^+}{u_\tau}\frac{\mu}{\rho} \tag{19}$$

The thickness of the first boundary layer can be calculated as:

$$\delta_{\text{tot}}=0.37d\cdot Re^{-0.2} \tag{20}$$

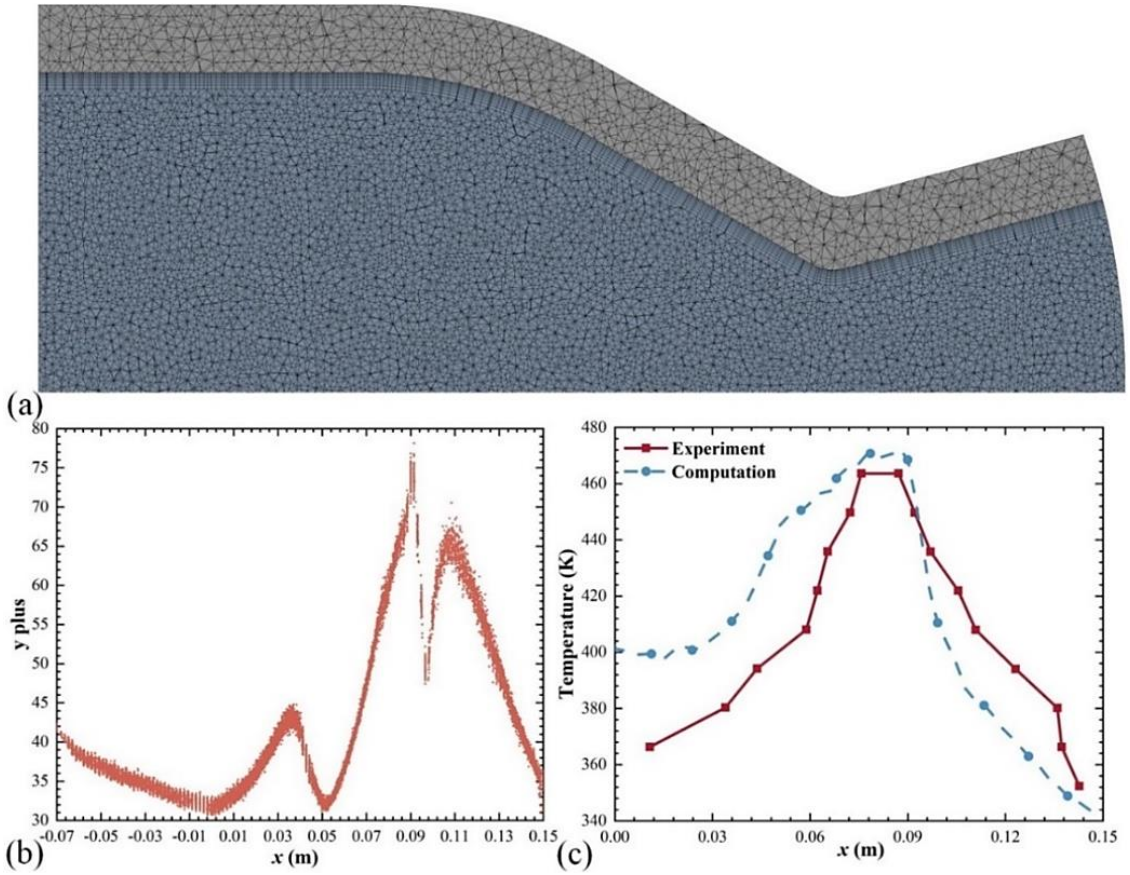

Fig. 3 Analysis of Converging-Diverging nozzle (a) Meshes (b) y^+ distribution (c) Comparison

$$\delta_{\text{tot}} = \delta_0 \left(\frac{r^N - 1}{r - 1} \right) \tag{21}$$

The growth rate of the boundary layer is 1.2, and the total number of boundary layers can be calculated as follows:

$$N = \frac{\lg\left(\frac{\delta_{\text{tot}}}{\delta_0}(r-1) + 1 \right)}{\lg(r)} \tag{22}$$

The mesh sizes for the fluid and solid fields are 2 mm and 3 mm, respectively. The mesh division and the corresponding y^+ distribution is presented in Fig. 3(a) and Fig. 3(b). Figure 3(c) compares the calculated inner wall temperature of the converging-diverging nozzle with experimental data (Back et al.,1964; Liu et al., 2005). In this comparison, the position x=0 corresponds to the throat of the nozzle. As shown in Fig. 3(c), the mathematical model's calculations align well with the experimental results, with a maximum error of approximately 10%. This outcome validates the accuracy of the mathematical model.

3. FLUID-THERMAL ANALYSIS FOR AVEN

3.1 Fluid Field Analysis Model

The working conditions for the AVEN are presented in Table 2. This study examines not only the influence of aerodynamic and thermal loads on the dynamic characteristics, but also the effect of vector deflection on the nozzle structure. The deflection angles investigated range from 0° to 20°, with the maximum deflection angle being determined by the physical design limitations of the nozzle, ensuring both safe operation and optimal aerodynamic performance. Consequently, fluid field and structural thermal analyses are conducted for deflection angles of 0°, 5°, 10°, 15°, and 20°.

Figure 4 illustrates the simplified solid field model of the AVEN. The inner wall surface is represented by the bottom of the convergence regulator plate, the expansion regulator plate, and the cruciform joint, while the radius of the frame is used as the inlet wall radius. It is important to note that the temperature field obtained through fluid field analysis reflects only the temperature distribution of the simplified model, rather than that of the actual components. To achieve a more accurate structural temperature field, the temperature from the fluid field calculation is used as the boundary condition for the thermal analysis. Thus, the primary goal of the fluid field analysis is to determine the pressure distribution at the fluid-structure interaction surface and the inner wall temperature with greater accuracy.

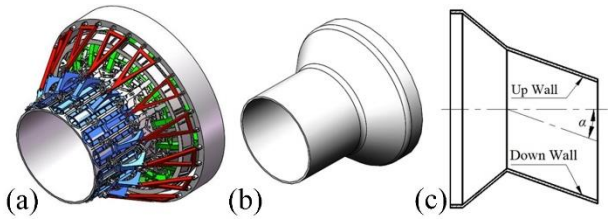

Fig. 4 AVEN simplified model (a) AVEN mechanism (b) Simplified model (c) Simplified Model Schematic

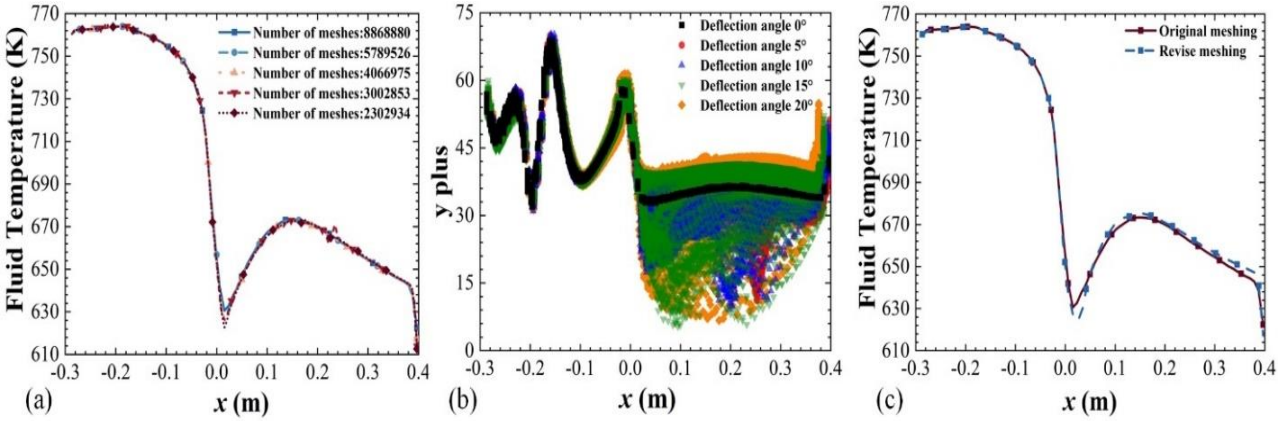

Fig. 5 Mesh independence verification (a) Mesh size (b) y^+ curve (c) Boundary layer mesh

Table 3 Actual division value of boundary layer mesh

Location	Thickness (mm)	Total number
Inlet section	0.1	20
Inlet section fillet	0.66	15
Convergence segment	7.5×10^{-2}	18
Throat fillet	6×10^{-2}	22
Expansion segment	5.5×10^{-2}	22

Table 4 Mesh independence verification table

Size (mm)	Elements	Nodes	y^+
6	8868880	2341145	31.6~82.2
7	5789526	1638848	32.3~80.3
8	4066975	1245325	32.5~73.1
9	3002853	994621	32.3~73.6
10	2302934	824955	31.9~68.9

3.2 Meshing Method of Fluid Field

This paper focuses on a high Re fluid field, employing an enhanced wall function. To obtain more accurate pressure and temperature values at the fluid-structure interaction surface, the condition $y^+\leq5$ or $30\leq y^+\leq300$ must be met. To minimize computational effort and time, the paper adopts the range $30\leq y^+\leq300$, aiming to keep y^+ as close to 30 as possible. The thickness of the first boundary layer, the total boundary layer thickness, and the total number of boundary layers can be initially estimated using Eqs. (17) to (23). Based on these estimates, the actual division parameters are provided in Table 3.

Taking a deflection angle of 0° as an example, mesh independence verification was performed. The fluid field mesh sizes were 6 mm, 7 mm, 8 mm, 9 mm, and 10 mm, while the solid mesh size was 5 mm. The corresponding numbers of nodes, elements, and y^+ values for each mesh division are listed in Table 4.

Using the temperature of the fluid field at the fluid-structure interaction surface as the verification object, Fig. 5(a) presents the temperature variation curve of the fluid field at the interaction surface under five different mesh sizes. Calculations show that the maximum error between two adjacent mesh sizes occurs at a distance of 0.26 m from the throat, with an approximate error of 0.99%. This result indicates that the calculation outcomes are not highly sensitive to mesh quality. To optimize both calculation time and computational effort, the fluid field mesh size for the numerical analysis of fluid-structure interaction in this paper is set to 10 mm.

Table 5 Mesh with different deflection angles

Angles (°)	Elements	Nodes	y^+
0	2302934	824955	31.9~68.9
5	2314332	831593	11.2~67.0
10	2303793	827812	9.2~70.3
15	2288489	824347	5.4~68.8
20	2261664	814490	6.7~69.0

Based on this mesh size, calculations are performed for five different deflection angles. The number of nodes, elements, and the corresponding y^+ values for the mesh divisions of the five deflection conditions are listed in Table 5. Table 5 shows that when the AVEN is deflected, the minimum value of y^+ is less than 30, which could introduce significant errors in the fluid field calculation. Figure 5(b) illustrates that the y^+ value is excessively low only at the expansion regulator plate segment. As a result, the boundary layer mesh at this segment is modified, as detailed in Table 6. The number of nodes, elements, and

Table 6 Boundary layer mesh modified values of expansion regulator plate segment

Location	Thickness (mm)	Total number
Expansion segment	0.305	10

Table 7 Modified mesh parameters for different deflection angles

Size (mm)	Elements	Nodes	y^+
0	2166507	742012	32.0~227.9
5	2171173	745380	32.6~282.8
10	2160080	741804	31.4~266.1
15	2145995	739416	32.6~269.5
20	2123187	730826	32.2~294.8

corresponding y+ values for the modified boundary layer mesh division are shown in Table 7.

Figure 5 (c) displays the maximum error in the fluid field temperature at the fluid-structure interaction surfacebefore and after the modification of the boundary layer mesh is approximately 1.58% for deflection angle of 0°. This result indicates that when y^+ is within a reasonable range, the boundary layer mesh size has little effect on the results. The modified boundary layer mesh can be used for the meshing of the fluid field analysis in this paper.

3.3 Fluid Field Analysis

Figures 6(a), (c), and (e) show that as the deflection angle increases, both the pressure and temperature on the upper wall of the fluid field at the fluid-solid interaction surface also increase. Figures. 6(b), (d), and (f) indicate that the deflection angle has minimal impact on the pressure and temperature at the upper wall inlet-throat section, with the most significant effect observed at the expansion regulator plate segment. At this segment, both pressure and temperature initially increase before decreasing as the deflection angle decreases.

Figure 7 illustrates the behavior of an oblique shock wave along the wall of the convergence regulator plate segment when the deflection angle is 0°. As the deflection angle increases from 0° to 20°, the shock wave direction adjusts accordingly, remaining aligned with the axis of the expansion regulator plate segment. Additionally, a separation zone of pressure and temperature appears on the lower wall, with the size of this zone expanding as the deflection angle increases.

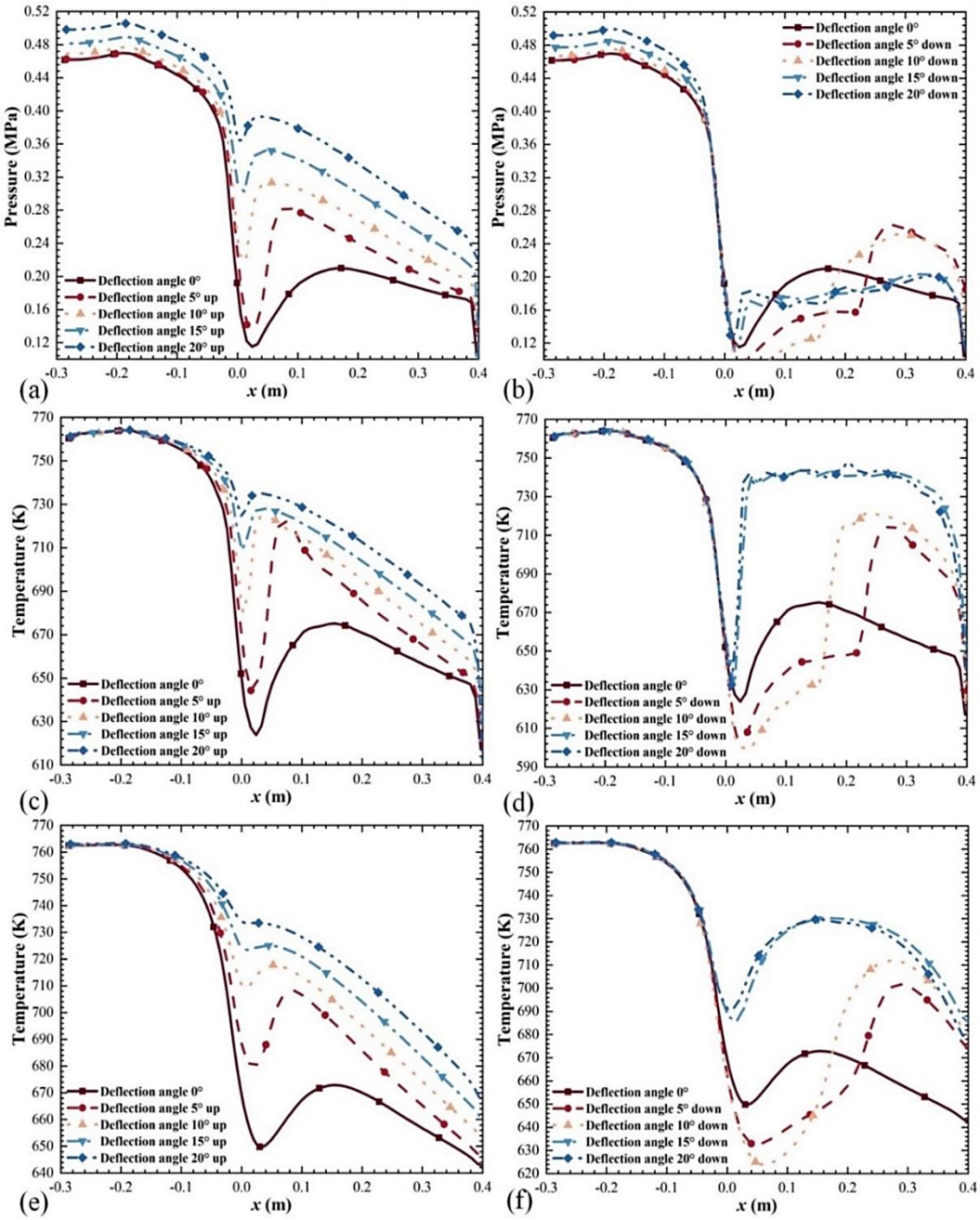

Fig. 6 Change curves of pressure and temperature at the fluid-solid interaction surface (a), (c), (e) Up wall (b), (d), (f) Down wall

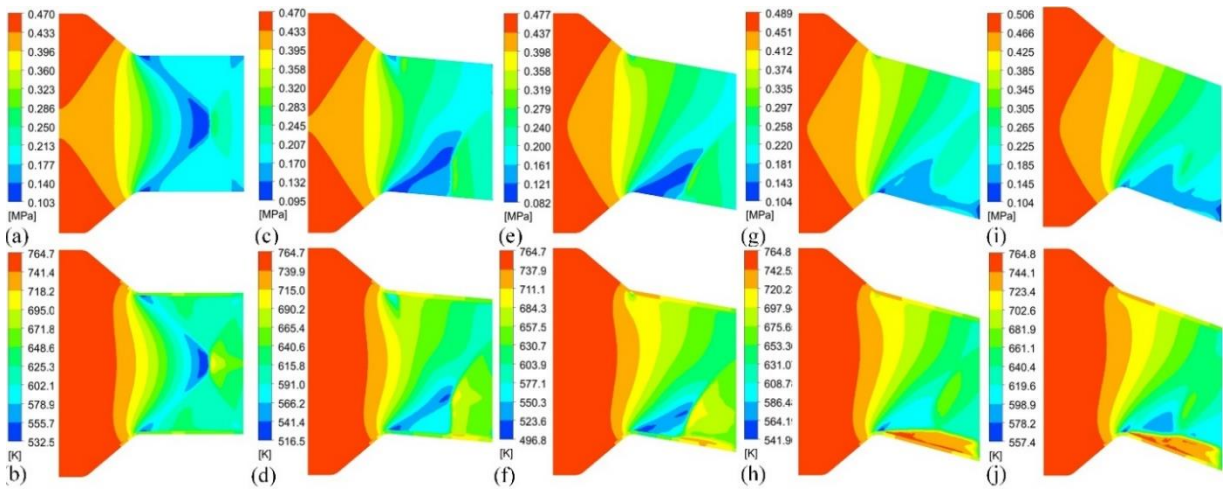

Fig. 7 Pressure and temperature distribution at the axisymmetric plane (a), (b) 0° deflection (c), (d) 5° deflection (e), (f) 10° deflection (g), (h) 15° deflection (i), (j) 20° deflection

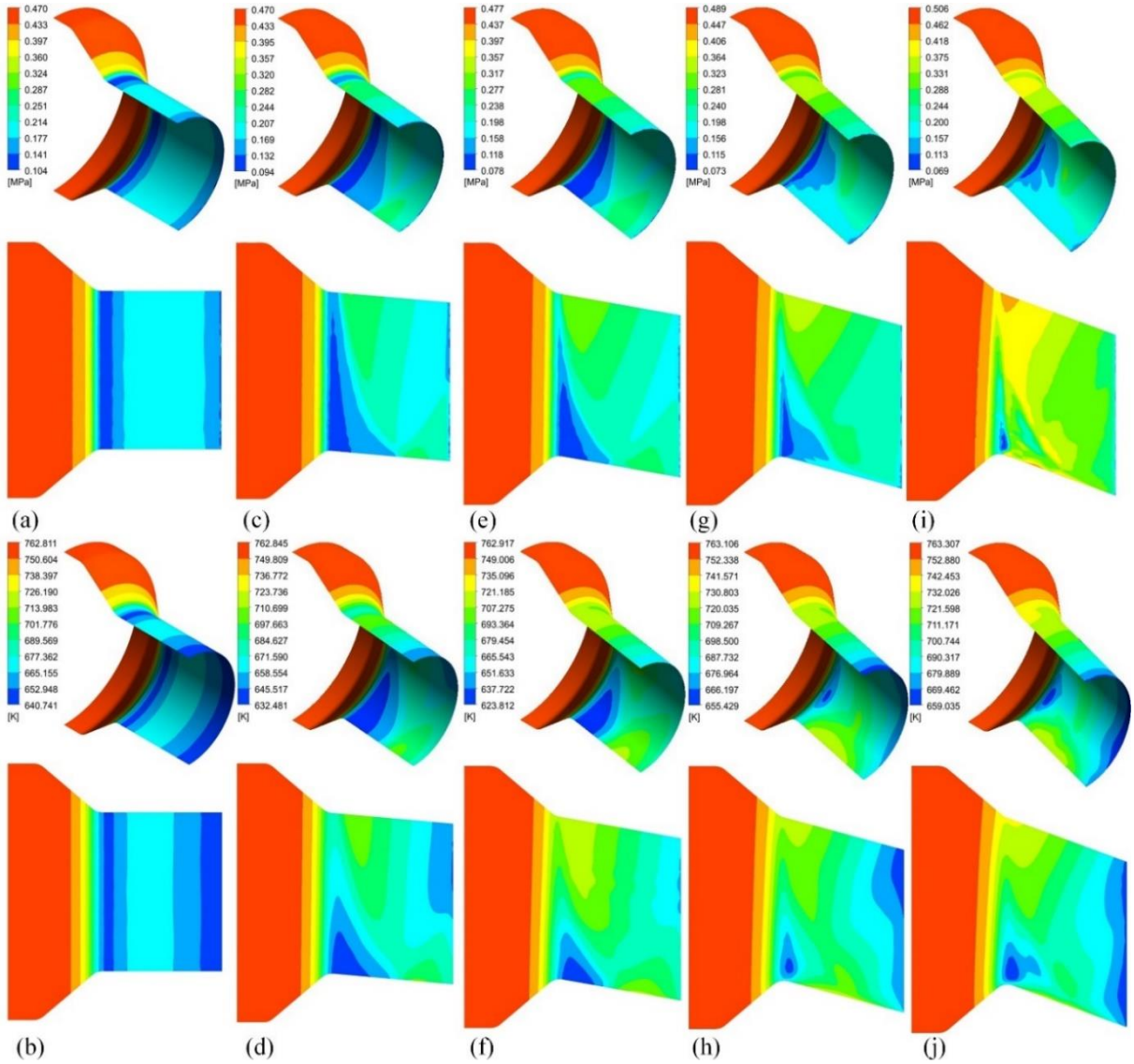

Fig. 8 Pressure and temperature distribution at the fluid-solid interaction surface (a), (b) 0° deflection (c), (d) 5° deflection (e), (f) 10° deflection (g), (h) 15° deflection (i), (j) 20° deflection

Figure 8 shows that as the deflection angle increases, the pressure at both the inlet section and the convergence regulator plate section undergoes minimal change. However, as the deflection angle increases further, the

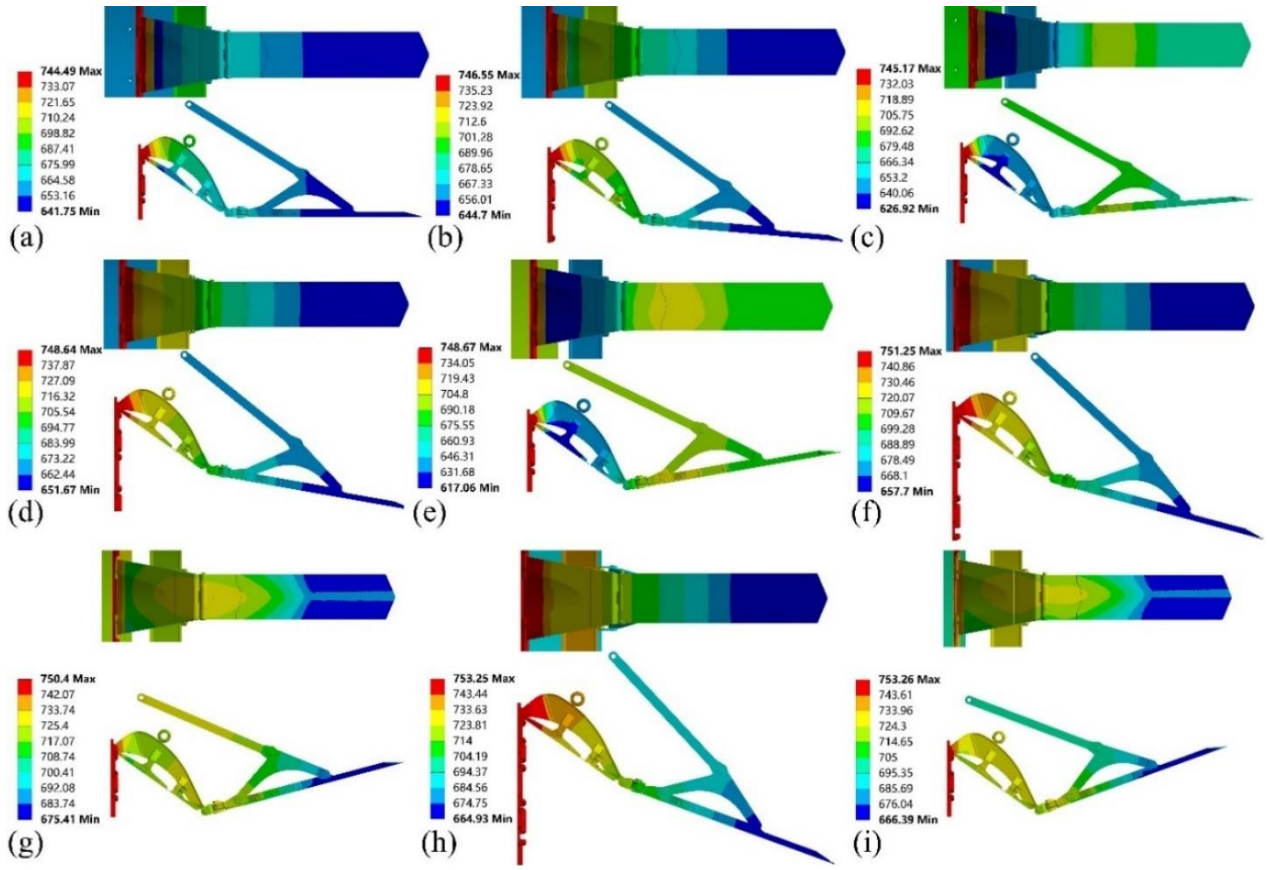

Fig. 9 Structural temperature distribution (Unit: K) (a) 0° deflection (b) 5° deflection (Up Wall) (c) 5° deflection (Down Wall) (d) 10° deflection (Up Wall) (e) 10° deflection (Down Wall) (f) 15° deflection (Up Wall) (g) 15° deflection (Down Wall) (h) 20° deflection (Up Wall) (i) 20° deflection (Down Wall)

area of maximum pressure expands while the area of minimum pressure decreases, causing the region of minimum pressure to shift downward along the throat. The variation in the inner wall temperature follows a similar trend to that of pressure. However, at the expansion regulator plate section, the temperature on the upper inner wall initially increases before decreasing as the deflection angle increases. This is due to the relationship between pressure and temperature in compressible flows, where a reduction in pressure generally leads to a decrease in temperature, and vice versa.

The pressure of the fluid field at the fluid-structure interaction surface and the temperature at the inner wall calculated in the fluid field analysis are used as the boundary conditions for dynamic analysis and structural thermal analysis, respectively.

3.4 Structural Thermal Analysis

Figure 9 illustrates the significant influence of the deflection angle on various components, including the convergence regulator plate, convergence skeleton, and cruciform joint on the upper wall, as well as the triangular rod, expansion bracket, and expansion convergence plate on the lower wall. As shown in Figs. 9(a), (b), (d), (f), and (h), an increase in the deflection angle corresponds to a rise in temperature at both the convergence regulator plate and the cruciform joint on the upper wall. The deflection angle, however, has minimal impact on the temperature of the expansion regulator plate on the upper wall. Moreover, as depicted in Figs. 9(a), (c), (e), (g), and (i), vector deflection leads to the formation of a temperature separation zone at the cruciform joint (throat), where the temperature at the axis center of the cruciform joint is elevated. This temperature separation zone refers to localized areas with significant temperature differences. This phenomenon primarily results from the interaction between high-velocity fluid flow and the nozzle geometry. As the deflection angle increases, the flow experiences both expansion and compression, leading to local flow separation, which in turn creates the temperature separation zone. The temperature separation zone can affect the nozzle's thermal distribution due to the uneven temperature distribution, which may influence the structural strength. As the deflection angle increases, the temperature of the convergence regulator plate, convergence skeleton, and cruciform joint on the upper wall also rises. In contrast, the temperature of the convergence regulator plate, convergence skeleton, and cruciform joint on the lower wall initially decreases before increasing again. Notably, at large deflection angles, a temperature separation zone appears, aligning with the temperature change trend at the fluid-solid interaction surface. Overall, the convergence regulator plate, being directly connected to the frame and exposed to high-temperature gas flow, experiences higher temperatures, as do the convergence frame and convergence regulator plate.

Table 8 Joint relationship between the main components

Component 1	Component 2	Constraints	Joint Number
Steering control ring	Ground	Translational	Joint 1
Triangle rod	Steering control ring	Revolute	Joint 2
Triangle ball hinge	Triangle rod	Spherical	Joint 3
Expansion bracket	Triangle ball hinge	Revolute	Joint 4
Expansion regulator plate	Expansion bracket	Revolute Translational	Joint 5 Joint 6
Cruciform joint	Expansion regulator plate	Fixed	Joint 7
Convergence regulator plate	Cruciform joint	Revolute	Joint 8
Convergence skeleton	Convergence regulator plate	Translational 1 Translational 2 Revolute 1	Joint 9 Joint 10 Joint 11
Convergence skeleton	Frame	Revolute	Joint 12
Convergence regulator plate	Frame	Revolute	Joint 13
Frame	Ground	Fixed Support	Joint 14
Roller	Convergence regulator ring	Revolute	Joint 15
Convergence regulator ring	Ground	Translational	Joint 16
Roller	Convergence skeleton	Friction	Contact 1

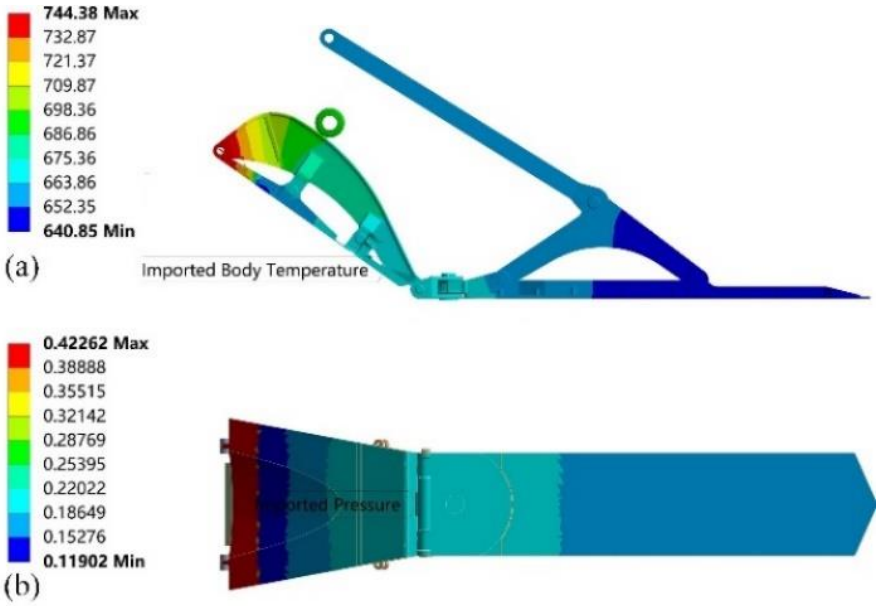

Fig. 10 External load boundary conditions (a) Temperature (Unit: K) (b) Pressure (Unit: MPa)

The structural temperature calculated through thermal analysis serves as the boundary condition for the dynamic analysis.

4. DYNAMIC CHARACTERISTICS OF AVEN

Based on the results of fluid field and structural thermal analyses, a dynamic analysis is conducted. Considering that the AVEN is influenced not only by driving loads but also by aerodynamic and thermal loads during operation, the effects of these loads on the dynamic characteristics are investigated. To reduce computational effort, the convergence regulator ring and the steering control ring are treated as rigid bodies, while the remaining components are modeled as flexible bodies. Building on this, the dynamic characteristics, accounting for both aerodynamic and thermal loads, are examined.

4.1 Boundary Conditions and Meshing

Since this paper only considers the upward and downward deflection of the nozzle, the joint between the cruciform joint and the expansion regulator plate is fixed. Table 8 illustrates the joint relationship, while Fig. 10 presents the external load boundary conditions.

Due to the lack of available friction coefficient data for the material used, a friction coefficient experiment was conducted at 12 rpm, 25,000 N, and 623.15 K (350°C) for 125 minutes. The experimental setup utilized a self-developed nozzle mechanism on a principle-level experimental bench, as shown in Fig. 11. This experimental bench is based on the prototype of the Axisymmetric Thrust Vectoring Nozzle mechanism and incorporates a convergent skeleton-roller moving component. The materials, processing accuracy, load

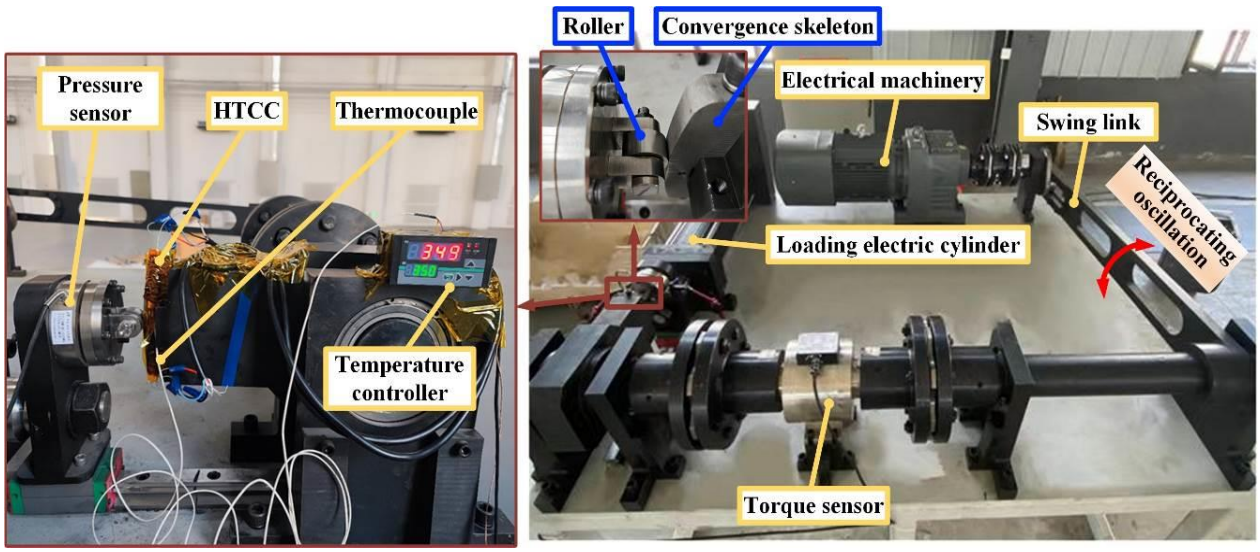

Fig. 11 Principle-level experimental bench for AVEN

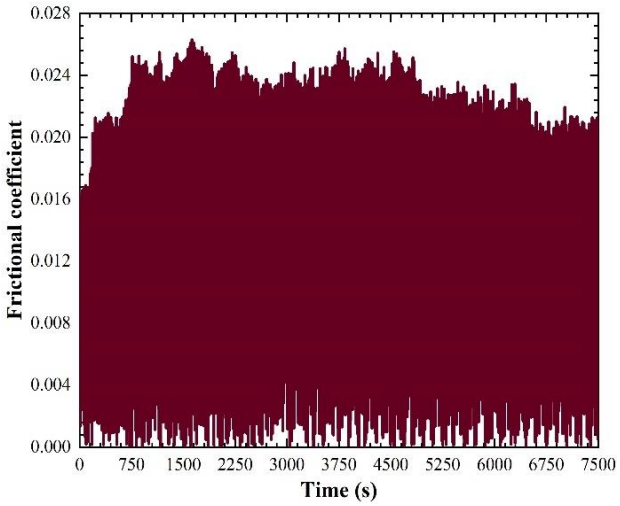

Fig. 12 Experimental result

form, and structural characteristics of the experimental setup are consistent with those of real aircraft engines.

As shown in Fig. 12, the results of the friction coefficient experiment are presented. The friction coefficient used in this study is the average value derived from the data in Fig. 12, which was calculated to be 0.014. This value is subsequently applied as the friction coefficient in the dynamic calculations.

To investigate the influence of aerodynamic and thermal loads on the dynamic characteristics, four cases, as shown in Table 9, are analyzed.

This paper primarily focuses on the analysis of key components, including the triangle rod, expansion regulator plate, roller, convergence skeleton, and convergence regulator plate.

4.2 Analysis of Calculation Results

As shown in Fig. 13, during the initial movement phase, the angular displacement curve of each joint exhibit oscillations. Due to this, the impact of aerodynamic and thermal loads on the AVEN cannot be analyzed with high accuracy at this stage. Therefore, the study focuses on the

Table 9 Different load cases

Case	Aerodynamic load	Thermal load	Case
Case 1	N	N (298.15K)	Case 1
Case 2	Y	N (298.15K)	Case 2
Case 3	N	Y	Case 3
Case 4	Y	Y	Case 4

stable section of the curve. Fig. 13 demonstrates that the loads do not affect the motion trend of the joints but influence their positions. Fig. 13(a) shows that, at the same moment, the relative rotational angle of Joint 2 under thermal load is smaller than that under no load, whereas the relative rotational angle under aerodynamic load is larger than under no load. The thermal load has a smaller effect on the relative rotational angle of Joint 2, while aerodynamic load is the primary influencing factor. Fig. 13(b) illustrates that, at the same moment, the relative rotational angle of Joint 4 under aerodynamic load is smaller than that under no load, while the relative rotational angle under thermal load is greater than under no load. Aerodynamic load is the main factor affecting the relative rotational angle of Joint 4, while thermal load is secondary. Figure 13(c) shows that, at the same moment, the relative rotational angle of Joint 8 under thermal load is greater than under no load. In this case, thermal load is the primary factor influencing the relative rotational angle, with aerodynamic load having minimal impact. Figure 13(d) indicates that, at the same moment, the relative rotational angle of Joint 12 is greater under both thermal and aerodynamic loads compared to no load, with aerodynamic load being the main influencing factor.

It can also be observed from Fig. 13 that although aerodynamic load and thermal load have different effects on different components, the sum of the relative rotational angle changes caused by thermal load and aerodynamic load is equal to the relative rotational angle change caused by the combined aerodynamic-thermal load. Based on this, the following function expression can be obtained

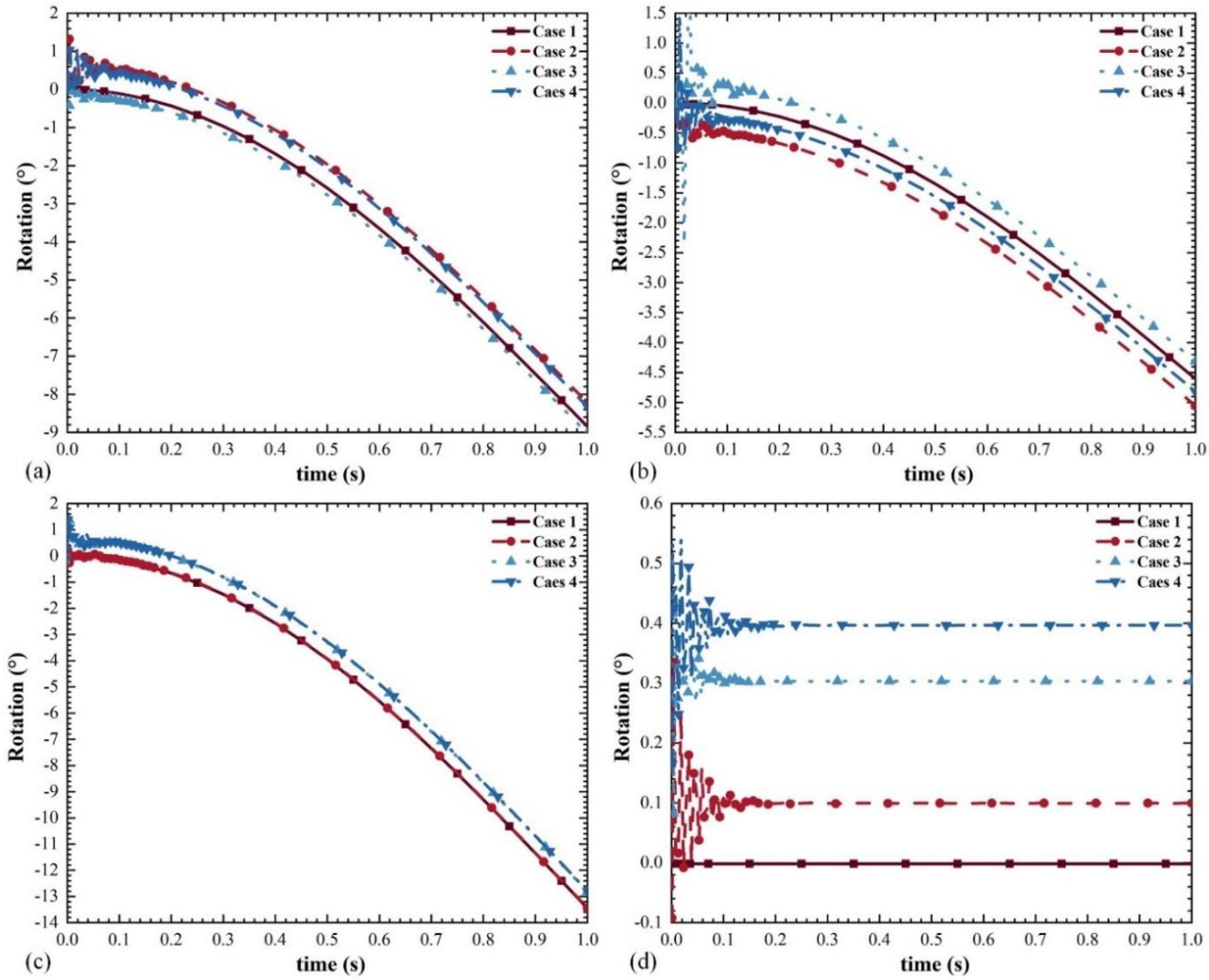

Fig. 13 Rotational angle variation curve (a) Joint 2 (b) Joint 4 (c) Joint 8 (d) Joint 12

Table 10 Maximum stress value of each component (Unit: MPa)

Object	Case 1	Case 2	Case 3	Case 4
Expansion regulator plate	0.25	1194.8	7.85	1196.4
Roller	6.04	909.84	2454.1	2301.2
Convergence skeleton	7.91	1257.3	2697	2683.5
Convergence regulator plate	33.69	533.48	4264	4338.6
Cruciform joint	29.98	332.95	26.48	320.2
Triangle rod	22.65	153.06	1.61	135.17
Expansion bracket	0.88	202.16	5.65	204.65
Triangle ball hinge	6.55	154.03	5.34	156.1

$$x_{PT_i} = x_{N_i} + \Delta x_{P_i} + \Delta x_{T_i} + \delta_e \tag{23}$$

As shown in Table 10, the aerodynamic load has the greatest impact on the structural stress in the C-segment, which includes the expansion regulator plate, cruciform joint, triangular rod, expansion bracket, and triangular ball hinge. In contrast, the thermal load significantly affects the convergence regulator ring segment, which includes the roller, convergence skeleton, and convergence regulator plate. This is primarily because the relative positioning between the frame and the convergence regulator ring is relatively fixed. As a result, the thermal expansion of the roller, convergence skeleton, and convergence regulator plate can cause adjacent components to press against each other, thereby increasing the structural stress. Furthermore, it is observed that the combined effect of aerodynamic and thermal loads is greater than that of either load acting independently.

Figure 14 illustrates that in all four cases, the location of maximum stress at the contact surface between the convergence skeleton and the roller remains generally consistent. The highest maximum stress occurs under the combined aerodynamic-thermal load. This is primarily due to the connection between the convergence skeleton

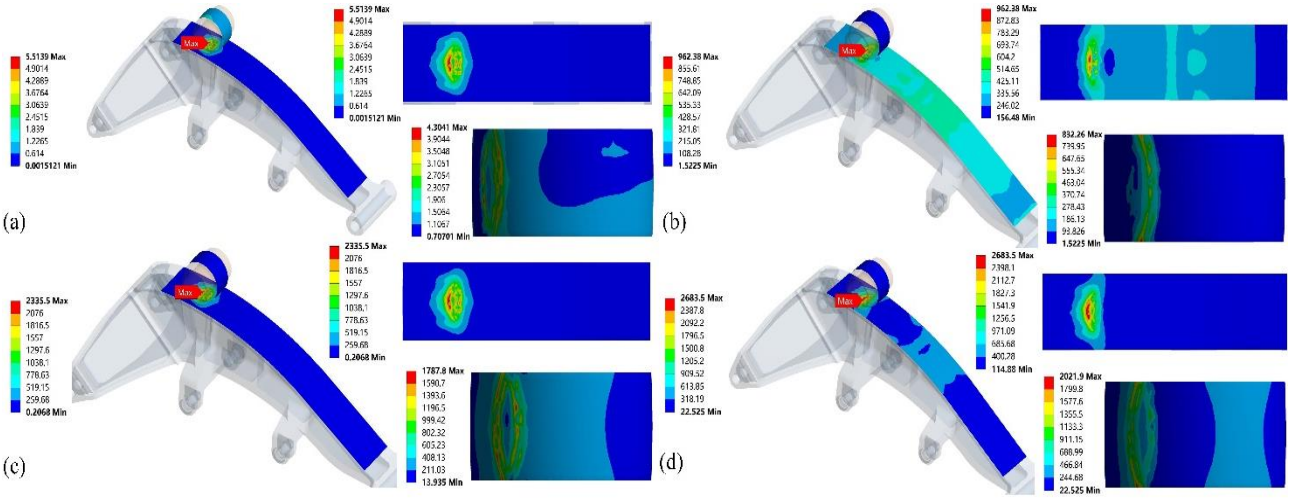

Fig. 14 Stress distribution of Contact 1 at t=1s (Unit: MPa) (a) Case 1 (b) Case 2 (c) Case 3 (d) Case 4

and the convergence regulator plate by a pin. When the convergence regulator plate is subjected to aerodynamic load, the force is transferred to the convergence skeleton, causing it to press against the roller, thereby increasing the load at the contact surface. Additionally, under thermal load, the thermal expansion causes the convergence skeleton and the roller to exert pressure on each other, further increasing the load and maximum stress at the contact surface. This revision streamlines the text and ensures clarity, while maintaining the technical details needed for a professional research paper.

5. CONCLUSION

This research investigates the dynamic characteristics of AVEN at various deflection angles, considering the effects of thermal and aerodynamic loads, alongside fluid field analysis, structural thermal analysis, and dynamic characteristic analysis. The following conclusions are drawn:

1. Fluid field analysis reveals that, as the deflection angle increases, significant changes in fluid pressure and temperature occur on the fluid-structure interaction surface, particularly around the expansion regulator plate and cruciform joints. Structural thermal analysis shows that thermal loads have a substantial impact on the temperature of components such as the convergence regulator ring, roller, and convergence skeleton. This leads to increased thermal expansion of these components, thereby raising the stress between adjacent parts.

2. Dynamic analysis indicates that while the load does not affect the motion trend of the joints, it does influence their motion positions. Both aerodynamic and thermal loads can alter the relative rotational angular displacement of AVEN joints, with thermal loads having a more pronounced effect on joints 8 and 12. Whether considering aerodynamic load, thermal load, or their combination, the trend in load changes significantly affects the motion position. The relative rotational angle of the joint is determined by the sum of the angle variations caused by both thermal and aerodynamic loads.

3. Stress analysis shows that aerodynamic loads significantly impact the stress on components like the steering control ring, expansion regulator plates, and cruciform joints, while thermal loads mainly affect the convergence regulator ring, roller, and convergence skeleton. Under the combined action of aerodynamic and thermal loads, the contact surface stress between the convergence skeleton and the roller increases significantly.

In conclusion, both aerodynamic and thermal loads have a substantial impact on the motion characteristics, structural stress, and joint forces in AVEN. In the design and optimization of AVEN, the combined effects of aerodynamic and thermal loads must be carefully considered. This paper provides a novel approach for the virtual design of AVEN.

ACKNOWLEDGEMENTS

This work was supported by the National Science and Technology Major Project [grant numbers J2019-IV-0002-0069]; the National Natural Science Foundation of China [grant numbers 12272089]; the Fundamental Research Funds for the Central Universities of China [grant numbers N2403004, N2224001-4, N2303002].

CONFLICT OF INTEREST

The authors declare no potential conflicts of interest with respect to the research, authorship/contribution, and publication of this original paper.

AUTHORS CONTRIBUTION

Sibo Yao: Conceptualization, Methodology, Software, Validation, Formal analysis, Investigation, Data Curation, Writing-original draft, Project administration, Funding acquisition. **Zhong Luo:** Conceptualization, Supervision, Writing-review&editing, Funding acquisition. **Hongwei Zhang:** Resources. **Chunyang Xu:** Conceptualization. **Haiyang Ji:** Writing-review. **Chao Pang:** Writing-review.

REFERENCES

Alimohammadi, H. R., & Aghaei-Togh, R. (2023). Multi-objective multidisciplinary design optimization of liquid-propellant engines thrust chamber based on a surrogate model. *Proceedings of the Institution of Mechanical Engineers, Part C: Journal of Mechanical Engineering Science*, *237*(14), 3215-3229. https://doi.org/10.1177/09544100231182268

Back, L. H., Massier, P. F., & Gier, H. L. (1964). Convective heat transfer in a convergent-divergent nozzle. *International Journal of Heat and Mass Transfer*, *7*(05), 549-568. https://doi.org/10.1016/0017-9310(64)90052-3

Bahamon, J., & Martinez, M. (2023). Study of fluid-dynamic behavior in a convergent–divergent nozzle by shape optimization using evolutionary strategies algorithms. *Proceedings of the Institution of Mechanical Engineers, Part C: Journal of Mechanical Engineering Science*, *237*(12), 2844-2862. https://doi.org/10.1177/09544100231163372

Chen, F., Liu, H., & Zhang, S. T. (2018). Time-adaptive loosely coupled analysis on fluid-thermal-structural behaviors of hypersonic wing structures under sustained aeroheating. *Aerospace Science and Technology*, *78*, 620-636. https://doi.org/10.1016/j.ast.2018.05.015

Chen, H. C., & Patel, V. C. (1988). Near-Wall turbulence models for complex flows including separation. *AIAA Journal*, *26*, 641-648. https://doi.org/10.2514/3.9948

Cheng, Y., Hu, R., & Wu, J. (2023). Pipeline fault simulation and control of a liquid rocket engine. *Proceedings of the Institution of Mechanical Engineers, Part C: Journal of Mechanical Engineering Science*, *237*(12), 2700-2719. https://doi.org/10.1177/09544100231157139

Christophe, B. (2018). *Turbulence*. National Defense Industry Press.

Edathol, J., Brezgin, D., Aronson, K., & Kim, H. D. (2020). Prediction of non-equilibrium homogeneous condensation in supersonic nozzle flows using Eulerian-Eulerian models. *International Journal of Heat and Mass Transfer*, *152*, 119451. https://doi.org/10.1016/j.ijheatmasstransfer.2020.119451

Gao, H., Zhai, J. Y., Zhang, H., Han, Q. K., & Liu, J. G. (2021). Dynamic investigation of a spatial multi-body mechanism considering joint clearance and friction based on coordinate partitioning method. *Proceedings of the Institution of Mechanical Engineers, Part C: Journal of Mechanical Engineering Science*, *235*(24), 7569-7587. https://doi.org/10.1177/09544062211025566 4

Gao, Y. G., Liu, Y., & Ma, D. (2022). Effect of operation pressure on heat release characteristics in solid rocket motor nozzle considering detailed chemical reaction mechanism. *Aerospace Science and Technology*, *128*, 107794. https://doi.org/10.1016/j.ast.2022.10779411

Jongen, T. (1992). *Simulation and modeling of turbulent incompressible flows*. Dissertation, EPF Lausanne.

Kowollik, D., Tini, V., Reese, S., & Haupt, M. (2013). 3D fluid-structure interaction analysis of a typical liquid rocket engine cycle based on a novel viscoplastic damage model. *International Journal for Numerical Methods in Engineering*, *94*(13), 1165-1190. https://doi.org/10.1002/nme.4488

Li, F. S. (2009). Backward solutions to Neumann and Dirichlet problems of heat-conduction equation. *Applied Mathematics and Computation*, *210*(1), 211-214. https://doi.org/10.1016/j.amc.2008.12.077

Li, H. W., Gao, Y. F., Du, C. H., & Hong, W. P. (2021). Numerical study on swirl cooling flow, heat transfer and stress characteristics based on fluid-structure coupling method under different swirl chamber heights and Reynolds numbers. *International Journal of Heat and Mass Transfer*, *173*, 121228. https://doi.org/10.1016/j.ijheatmasstransfer.2021.121228

Li, W. H., Liu, T. H., Zhang, J., Chen, Z. W., Chen, X. D., & Xie, T. Z. (2017). Aerodynamic study of two opposing moving trains in a tunnel based on different nose contours. *Journal of Applied Fluid Mechanics*, *10*(5), 1375-1386. https://doi.org/10.18869/acadpub.jafm.73.242.27738

Li, Y. T., & Wang, Y. X. (2014). Eliminating singularity of a parallel driving mechanism of axisymmetric vectoring exhaust nozzle. *Proceedings of the Institution of Mechanical Engineers Part G-Journal of Aerospace Engineering*, *228*(12), 2300-2309. https://doi.org/10.1177/09544100135151115

Lijo, V., Kim, H. D., Rajesh, G., & Setoguchi, T. (2010a). Numerical simulation of transient flows in a vacuum ejector-diffuser system. *Proceedings of the Institution of Mechanical Engineers Part G-Journal of Aerospace Engineering*, *224*(7), 777-786. https://doi.org/10.1243/09544100JAERO680

Lijo, V., Kim, H. D., Setoguchi, T., Toshiaki, S., & Shigeru, M. (2010b). Numerical simulation of transient flows in a rocket propulsion nozzle. *International Journal of Heat and Fluid Flow*, *31*(3), 409-417. https://doi.org/10.1016/j.ijheatfluidflow.2009.12.005

Liu, Q. Y., Luke, E. A., & Cinnella, P. (2005). Coupling heat transfer and fluid flow solvers for multidisciplinary simulations. *Journal of Thermophysics and Heat Transfer*, *19*(4), 417-427. https://doi.org/10.2514/1.1352212

Liu, Y., Wang, H. F., Ma, D., Gao, Y. G., & Zhao, W. (2022). Numerical investigation of surface roughness effects on non-equilibrium flow in expansion section of rocket nozzle. *Aerospace Science and Technology*, *124*, 107523. https://doi.org/10.1016/j.ast.2022.1075239

Luo, Z., Song, Y. H., Ge, C. C., & Xu, C. Y. (2021). Fluid-solid-thermal coupling characteristics of ejector valve adjusting structure. *Journal of Northeastern*

University (Natural Science), 42(1), 75-82. (in Chinese) https://doi.org/10.12068/j.issn.1005-3026.2021.01.012

Nie, X., Zhu, Z. H., Liao, H. B., Zhang, Y. Z., & Xu, J. R. (2022). A Comparative study of the buoyancy-opposed wall jet using different turbulent models. *Journal of Applied Fluid Mechanics*, *15*(1), 85-98. https://doi.org/10.47176/jafm.15.0.32762

Pizzarelli, M., Cegan, A., Battista, F., & Nasuti, F. (2024). Application of semiempirical correlations for multidimensional heat transfer in rocket engine cooling channels. *Applied Thermal Engineering*, *254*(1), 123816. https://doi.org/10.1016/j.applthermaleng.2024.123816

Pizzarelli, M., Nasuti, F., & Onofri, M. (2014). Effect of cooling channel aspect ratio on rocket thermal behavior. *Journal of Thermophysics and Heat Transfer*, *28*(3), 410-416. https://doi.org/10.2514/1.T429915

Pizzarelli, M., Nasuti, F., Paciorri, R., & Onofris, M. (2009). Numerical analysis of three-dimensional flow of supercritical fluid in cooling channels. *AIAA Journal*, *47*, 2534-2543. https://doi.org/10.2514/1.3854214

Rogowski, K., Hansen, M. O. L., & Lichota P. (2018). 2-D CFD Computations of the Two-Bladed Darrieus-Type Wind Turbine. *Journal of Applied Fluid Mechanics*, *11*(4), 835-845. https://doi.org/10.29252/jafm.11.04.28383

Schlichting, H., & Gersten, K. (2017). *Boundary-layer theory*. Springer-Verlag. https://link.springer.com/book/10.1007/978-3-662-52919-5

Tahani, M., & Moradi, M. (2016). Aerodynamic investigation of a wind turbine using CFD and modified BEM methods. *Journal of Applied Fluid Mechanics*, *9*(1), 107-111. https://doi.org/10.36884/jafm.9.SI1.25820

Wang, H. P., Zhang, Y. B., & Yang, M. (2011). Flexible multi-body dynamics simulation of cold state axial-symmetric vectoring exhaust nozzle. *Journal of Aerospace Power*, *26*(11), 2427-2432. https://doi.org/10.13224/j.cnki.jasp.2011.11.0243

Wang, Y. S., Xu, J. L., Huang, S., Lin, Y. C., & Jiang, J. J. (2019). Computational study of axisymmetric divergent bypass dual throat nozzle. *Aerospace Science and Technology*, *86*, 177-190. https://doi.org/10.1016/j.ast.2018.11.05910

Wang, Y. X. (2006). *Axial-Symmetric Vectoring Exhaust Nozzle for Jet-Thrust-Aircraft*. National Defense Industry Press.

Wolfshtein, M. (1969). The velocity and temperature distribution of one-dimensional flow with turbulence augmentation and pressure gradient. *International Journal of Heat and Mass Transfer*, *12*, 301-318. https://doi.org/10.1016/0017-9310(69)90012-X

Xiang, J. X., & Sun, B. (2018). Research on coupled heat transfer of film cooling in LOX/GH2 thrust chambers. *Journal of Thermal Science and Technology*, *13*(2), T35. https://doi.org/10.1299/jtst.2018jtst0035

Xiang, J. X., Sun, B., Wang, T. P., & Yuan, J. Y. (2020). Effects of angled film-cooling on cooling performance in a GO2/GH2 subscale thrust chamber. *Applied Thermal Engineering*, 166, 114627. https://doi.org/10.1016/j.applthermaleng.2019.114627

Yan, M. G. (2002). *China aviation materials handbook*. Standards Press of China.

Yao, S. B., Luo, Z., Wei, K., Sun, Y. H., & Xu, C. Y. (2022). Analysis of fluid-solid-thermal coupling characteristics of axial-symmetric vectoring exhaust nozzle. *Proceedings of the Institution of Mechanical Engineers, Part C: Journal of Mechanical Engineering Science*, *236*(17), 9472-9484. https://doi.org/10.1177/0954406222109791118

Zhang, H., Wu, Q., Hao, Z., Meng, L., Luo, Z., Han, Q. (2024). Analysis of the dynamic of vector nozzle adjustment mechanism considering the effect of joint clearance. *Journal of Vibration Engineering & Technologies*, *12*, 6137-6154. https://doi.org/10.1007/s42417-023-01243-6

Zhang, Q., & Hisada, T. (2004). Studies of the strong coupling and weak coupling methods in FSI analysis. *International Journal for Numerical Methods in Engineering*, *60*(12), 2013–2029. https://doi.org/10.1002/nme.1034

Zhou, D., Lu, Z. L., Guo, T. Q., Shen, E. N., Wu, J. P., & Chen, G. P. (2020). Fluid-thermal modeling of hypersonic vehicles via a gas-kinetic BGK scheme-based integrated algorithm. *Aerospace Science and Technology*, *99*, 105748. https://doi.org/10.1016/j.ast.2020.105748

Zhou, S., Gao, H., Xu, C., Jia, Z., Lin, J., Han, Q., Luo, Z. (2022) Kinematic modeling and stiffness analysis of a 3-DOF 3SPS+3PRS parallel manipulator. *Mathematics*, *10*(23), 4465. https://doi.org/10.3390/math10234465